# Second harmonic generating (SHG) nanoprobes for in vivo imaging

**Periklis Pantazis[1], James Maloney, David Wu, and Scott E. Fraser**

Beckman Institute (139-74), Division of Biology, California Institute of Technology, Pasadena, CA 91125

Edited* by Harry B. Gray, California Institute of Technology, Pasadena, CA, and approved July 1, 2010 (received for review April 9, 2010)

**Fluorescence microscopy has profoundly changed cell and molecular biology studies by permitting tagged gene products to be followed as they function and interact. The ability of a fluorescent dye to absorb and emit light of different wavelengths allows it to generate startling contrast that, in the best cases, can permit single molecule detection and tracking. However, in many experimental settings, fluorescent probes fall short of their potential due to dye bleaching, dye signal saturation, and tissue autofluorescence. Here, we demonstrate that second harmonic generating (SHG) nanoprobes can be used for in vivo imaging, circumventing many of the limitations of classical fluorescence probes. Under intense illumination, such as at the focus of a laser-scanning microscope, these SHG nanocrystals convert two photons into one photon of half the wavelength; thus, when imaged by conventional two-photon microscopy, SHG nanoprobes appear to generate a signal with an inverse Stokes shift like a fluorescent dye, but with a narrower emission. Unlike commonly used fluorescent probes, SHG nanoprobes neither bleach nor blink, and the signal they generate does not saturate with increasing illumination intensity. The resulting contrast and detectability of SHG nanoprobes provide unique advantages for molecular imaging of living cells and tissues.**

animal imaging | nonlinear crystals | organic dyes | quantum dots

Synthetic chemistry and molecular genetics have revolutionized fluorescence microscopy techniques by offering a wide range of dyes with varied fluorescence properties, creating means to tag defined sites in a target protein, and generating a wide range of genetically encoded fluorescent proteins, based on the GFP from the jellyfish *Aequorea victoria* (1) and other fluorescent proteins (reviewed in ref. 2). For example, fusions of a GFP color variant with the coding sequence of a protein offers a direct means to analyze the expression of that protein, as well as to follow the localization of the protein or the dynamics of labeled cell populations (3, 4). Similarly, chemical dyes or quantum dots can be used to label defined targets by inserting a sequence into the coding sequence of the protein that encodes an attachment site (e.g., a biotinylation target sequence or a ligand sequence) or by integrating a nonnatural amino acid, either of which can direct the linkage of a target biomolecule to a fluorescent probe (5, 6). These techniques present the promise of molecular imaging in cells, tissues, and whole organisms, as they offer a means to introduce fluorescent probes in a controlled fashion; however, compromises in the performance of any fluorescent dye make it challenging to achieve this promise, especially in intact cells and tissues.

Although modern fluorescent probes offer a growing set of advantages, molecular imaging with fluorescent dyes, quantum dots, or genetically encoded fluorescent proteins must contend with limitations intrinsic to the label itself. These include the following:

1. Dye saturation, a limitation in the maximum number of photons that can be emitted in a given time, resulting from the finite excited state lifetime of any fluorophore (~5 ns). No matter how intense the exciting light, the dye cannot be fruitfully excited until the dye has emitted a photon or has otherwise returned to the ground state.
2. Dye bleaching, a limitation in the total number of photons that can be emitted by a dye in biological settings. This destructive process results from the low but significant probability that the dye will be excited to a reactive state that directly or indirectly destroys the dye. Bleaching is often the result of interstate conversion, exciting the dye into a triplet state that cannot return to the ground state by emitting a fluorescence photon; the triplet state is highly reactive with molecular oxygen, resulting in the creation of radical species that can destroy the dye or nearby components (a major source of phototoxicity).
3. Blinking, a dramatic fluctuation in the fluorescence from a transition of the fluorescent probe to a dark state that cannot generate emitted photons. Blinking is especially prominent in quantum dots, stochastically creating blocks of time during which the tagged molecule cannot be imaged. Although blinking has been minimized in some quantum dot (QD) formulations, this improvement comes with other limitations, such as a much broader emission spectrum.

Bleaching is the most commonly discussed of these factors, as it limits the length of time that biological targets can be studied due to loss of the label or to phototoxicity; however, blinking and saturation restrict performance as well, because they define the nature and magnitude of the signal that can be obtained from a single molecular probe. Given that a molecular imaging probe must generate a sufficient number of photons in each frame of an image sequence to be detected above background noise (typically autofluorescence from cellular and tissue components) and to be localized accurately, the light flux from a label is key to a successful experiment (7). Typical approaches to increase signal-to-noise (SNR) of fluorescent probe imaging by using more selective detection filters reduce the fraction of probe fluorescence that is captured; this loss cannot be compensated for by turning up the exciting laser due to increased photobleaching and increased autofluorescence.

To circumvent the above issues with fluorescent probes, we decided to investigate probes that can perform second harmonic generation (SHG). SHG is a second-order nonlinear optical process in which two photons at the frequency $\omega$ interacting with noncentrosymmetrical media (i.e., material lacking a generalized mirror symmetry) combine to form a new photon with twice the energy, and therefore twice the frequency ($2\omega$) and half the wavelength of the initial photons (8, 9) (Fig. 1). The optical response of the media can be described by expressing the induced polarization $P(\omega)$ as a power series of the optical field strength $E(\omega)$ of the incident light:

Author contributions: P.P. and S.E.F. designed research; P.P. and J.M. performed research; P.P. contributed new reagents/analytic tools; P.P. and D.W. analyzed data; and P.P. and S.E.F. wrote the paper.

Conflict of interest statement: This work is the subject of patent applications filed by the California Institute of Technology.

*This Direct Submission article had a prearranged editor.

[1]To whom correspondence should be addressed at: Beckman Institute (139-74), Division of Biology, California Institute of Technology, 1200 East California Boulevard, Pasadena, CA 91125. E-mail: pantazis@caltech.edu.

This article contains supporting information online at www.pnas.org/lookup/suppl/doi:10.1073/pnas.1004748107/-/DCSupplemental.

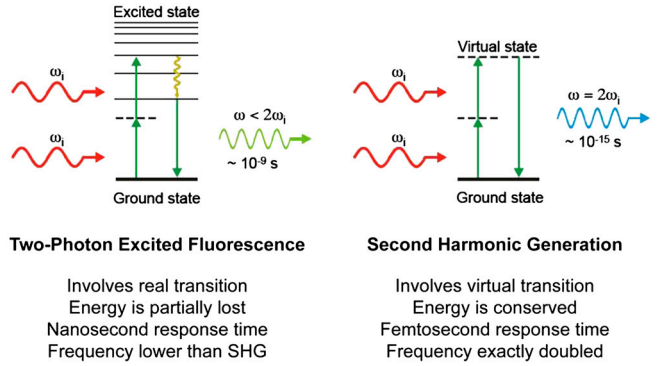


**Fig. 1.** Two-photon excited fluorescence versus SHG. Displayed are the Perrin–Jablonski fluorescence diagram (*Left*) and the energy-level diagram (*Right*) describing two-photon excited fluorescence and SHG, respectively. When intense light is shone on materials that do not possess an inversion symmetry, the vibrating electric field of the incident beam results in the polarization of the medium, reemitting light at the original frequency $\omega_i$ but also at the frequency $2\omega_i$ (here shown, *Right*) that is twice the original one (with half of the wavelength). Unlike two-photon excited fluorescence, all of the incident radiation energy at frequency $\omega_i$ is converted in the process of SHG to radiation at the SHG frequency $2\omega_i$. And whereas two-photon excited fluorescence involves real energy transition of electrons, SHG involves only virtual energy transition. As a result, using ultrafast (femtosecond) pulsed lasers, the response time of SHG is at the femtosecond level, about several orders of magnitude faster than the nanosecond response time of fluorescence, allowing very fast and sensitive detection.

$$P(\omega) = \chi^{(1)} \cdot E(\omega) + \chi^{(2)} \cdot E(\omega)^2 + \chi^{(3)} \cdot E(\omega)^3 + \cdots$$

The coefficient $\chi^{(n)}$ is the $n$th-order susceptibility of the material, $\chi^{(1)}$, $\chi^{(2)}$, and $\chi^{(3)}$ corresponding to optical effects such as absorption or reflection, SHG, and third harmonic generation, respectively. With such symmetry constraints, SHG is best produced from structures without inversion symmetry combined with a high degree of organization and orientation, such as anisotropic crystals or endogenous structural protein arrays in tissue.

SHG microscopy is an emerging microscopic technique for a wide range of biological and medical imaging because some endogenous proteins, such as collagen fibrils in connective tissues or the actomyosin lattice of muscle cells (10), are sufficiently ordered to generate detectable SHG. The intrinsic signal generated by structured arrays of these proteins permits SHG microscopy to image a variety of tissue structures noninvasively. As a nonlinear optical process, SHG shares many features with two-photon excited fluorescence: Both depend on two photons striking a site at once, and therefore the efficiency of both SHG emission and two-photon fluorescence depends on the square of the excitation intensity. Because the intensity increases dramatically at the focus of a microscope objective, falling off by the square of the distance, the efficiency of both processes falls off by the fourth power of the distance from the focus, offering optical sectioning without the need for a confocal aperture. Both techniques employ pulsed lasers in the infrared wavelength range, permitting deeper optical penetration and reduced nonspecific phototoxicity compared to one-photon excitation (11). These properties are of vital importance for long time-lapse imaging. However, unlike two-photon excited fluorescence in which the fluorescent dye can saturate, bleach, and/or generate toxic by-products, SHG is a coherent process involving only virtual energy transitions with none of the negative consequences of a finite excited state lifetime (Fig. 1).

## Results and Discussion

To define a versatile and durable SHG labeling probe for biological systems, we investigated several noncentrosymmetric nanocrystals that have been reported to have large second-order nonlinear optical susceptibilities, $\chi^{(2)}$ (12–15). We screened candidates for their expected stability in physiological conditions and their possible toxicity to cells, and found that tetragonal barium titanate ($BaTiO_3$) was stable and had a strong SHG signal in vivo. Unlike the SHG from endogenous protein arrays, which is much weaker than two-photon excited fluorescence, $BaTiO_3$ created strong SHG at moderate to low peak illumination intensities of around $10^9$ $Wcm^{-2}$ (see *Materials and Methods*). This illumination level is at least 100 times lower than the tissue damage threshold (16) and comparable to the illumination used in two-photon laser-scanning microscopy (TPLSM) (17). Furthermore, we found that the nanocrystals emitted strong SHG multidirectionally (unlike the forward-directed SHG of bulk materials and endogenous protein arrays), permitting the microscope objective lens to both illuminate the specimen and to collect the SHG signal, just as in TPLSM. These results suggested that $BaTiO_3$ would be an excellent test case for the use of SHG nanoprobes as a biological imaging agent.

The SHG signal from $BaTiO_3$ nanocrystals was spectrally well-defined (Fig. 2*A*). Illuminating the 30-nm $BaTiO_3$ nanocrystals (Fig. 2*A Inset*) at 820 nm with a conventional two-photon microscope yielded an SHG signal profile with a discrete peak at 410 nm. The spectral detector (LSM 510 META) used for this analysis has limited spectral resolution and may well overestimate the SHG FWHM. The expected FWHM of the SHG is $1/\sqrt{2}$ the bandwidth of the ultrafast pulsed laser used to illuminate the specimen (~5 nm). This spectral width is significantly narrower than the FWHM of fluorescence labels, including QDs (18, 19), and dramatically narrower than the broad, multipeaked spectra generated by a new generation of QDs reported to have less blinking (20). Furthermore, the signal generated by the $BaTiO_3$ nanocrystals was stable over several hours of illumination, and the properties were environmentally insensitive when tested in various organic solvents (e.g., methanol, toluene) or in aqueous solutions over a wide range of salt concentrations (0.1–2.0 M). These narrow emission and stable spectral properties permit the use of optimized emission filters with very narrow bandwidths that can block most of the broad and longer-wavelength endogenous autofluorescence from biological tissues (see below).

To better define the frequency conversion efficiency (21) of $BaTiO_3$ nanocrystals, we examined the SHG generated for a variety of excitation wavelengths (*SI Materials and Methods* and Fig. S1*A*). As the excitation wavelength was increased from 780 to 970 nm in a conventional TPLSM, the wavelength of the SHG signal from the $BaTiO_3$ nanocrystals increased from 390 to 485 nm. The intensity of the SHG from nanocrystals was more wavelength dependent than might be expected from measurements of bulk materials, with the highest efficiency achieved at shorter excitation wavelengths. This difference was not because of different bandwidths, pulsewidths, or sensitivities of the laser, the associated optics, or the TPLSM. Consistent with this intensity profile being due to the properties of the $BiTiO_3$ rather than an experimental limitation, our experiments showed that the SHG susceptibilities of different noncentrosymmetric nanomaterials (Fig. S1*A*) varied with wavelength significantly. The optimal wavelength range is broadest for $BiTiO_3$ in comparison with the other nanocrystals investigated, making it detectable at longer illumination wavelengths. These material-specific signal characteristics offer a simple means for multilabel SHG imaging, discriminating between two different types of nanocrystals by recording the SHG signal intensities at two or three distinct excitation wavelengths (e.g., 800 versus 880 nm; Fig. S1 *B* and *C*).

**Blinking.** An important part of biological imaging is the detection and tracking of individual molecules in biological systems with high spatial resolution in physiological conditions. Both QDs and single fluorescent molecules display "blinking," an intrinsic fluorescence intermittency most pronounced in QDs (22), which makes it challenging to track individual target molecules (23) and

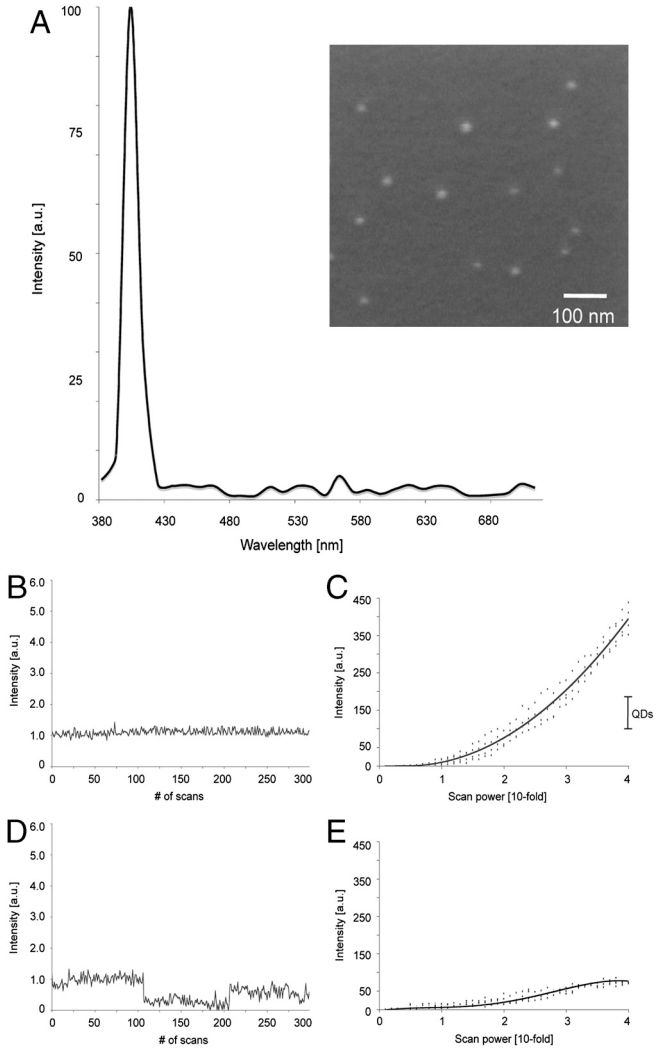


**Fig. 2.** SHG nanoprobes signal properties. (*A*) Displayed is the normalized SHG signal spectrum of $BaTiO_3$ nanocrystals of the size of around 30 nm (*Inset*, SEM picture of $BaTiO_3$ nanocrystals) immobilized in 20% polyacrylamide gel (signal ranging from 380 to 710 nm) generated by tuning the excitation wavelength to 820 nm. (*B*) $BaTiO_3$ nanocrystal immobilized in 20% polyacrylamide gel and illuminated with low-intensity levels of 820 nm light 300 times with a scanning speed of 20 frames/s. The SHG signal intensity of $BaTiO_3$ is constant and does not display blinking. (*C*) $BaTiO_3$ nanocrystals were immobilized in 20% polyacrylamide gel and rapidly illuminated with gradually increasing 820-nm light intensity. The SHG signal intensity of $BaTiO_3$ nanocrystals increases quadratically. The dots show independent experimental results, whereas the line is a quadratic fit for $BaTiO_3$ ($n = 4$). Bar shows direct comparison of the obtained intensity range of QDs (see *E*) when rapidly illuminated under comparable conditions with increasing (up to 40-fold) 820-nm light intensity. (*D*) Water-soluble CdSe/ZnS QD immobilized in 20% polyacrylamide gel and illuminated with low-intensity levels of 820-nm light 300 times with a scanning speed of 20 frames/s. In contrast to $BaTiO_3$, the QD signal fluctuates displaying subblinking as well as major blinking. (*E*) QDs were immobilized in 20% polyacrylamide gel and rapidly illuminated with gradually increasing 820-nm light intensity. Signal saturation of the QD fluorescence occurs at very low-power levels. The dots show independent experimental results, whereas the line is a polynomial fit for QDs ($n = 4$).

complicates data analysis (24). As expected from the distinct photophysics of SHG, SHG nanoprobes do not display blinking. To optimize our conditions so that single nanocrystals could be studied, we ultrasonicated and nanofiltered the samples resulting in well-isolated nanocrystals, as confirmed using atomic force microscopy (Fig. S2*A*). The samples were immediately immobilized in 20% polyacrylamide before there was an opportunity for the nanocrystals to recluster. The blinking states of the QDs offer an easy means to validate that this procedure resulted in single, isolated particles; to avoid being misled by any rare clusters of SHG nanocrystals, only the dimmest particles were analyzed. For quantitative imaging, the microscope was flat-fielded, correcting for spatial aberrations in illumination and viewing optics as well as detector sensitivity (25) (see *SI Materials and Methods*, Fig. S2 *B* and *C*). Image series at 20 frames per second (Fig. 2*B* and Movie S1) show that the immobilized $BaTiO_3$ nanocrystals do not exhibit blinking behavior when analyzed over periods ranging from 15 s (Fig. 2*B*) to several hours. In contrast, QDs immobilized and imaged in the same fashion demonstrate pronounced blinking behavior with large fluorescence intensity changes between the bright and dark states (Fig. 2*D* and Movie S1), as previously described (26–28).

**Bleaching.** Because SHG involves only virtual energy transitions, SHG nanoprobes are not excited to a higher energy state and do not require any internal relaxation to achieve the Stokes shift between the excitation and emission maxima, in contrast to fluorescent probes. Time series images for periods of seconds to hours showed no decrement of the SHG signal from the nanocrystals, in dramatic contrast to the time-course data collected from the QDs (see above) and organic dyes. The short- and long-term stability of the intensity recorded from the nanocrystals reveals that the SHG nanoprobes neither bleach nor blink.

**Saturation and Single-Probe Intensity.** When imaging a low-abundance molecular target, the number of photons collected per unit time sets limits on sensitivity, SNR, and rapidity of acquisition. Common fluorescent probes (organic dyes or GFP) used as molecular reporters are limited in the number of photons they can emit due to dye saturation. Although QDs exhibit enhanced photostability (decreased bleaching) than most fluorescent probes, all QDs, including the recently introduced nonblinking quantum dots (20), possess finite excited state lifetimes, resulting in dye saturation as the excitation intensity is increased (29). To improve the signal, long integration times must be used, sacrificing temporal and spatial resolution (30). Quantitative imaging of the signal from single nanocrystals confirms the presence of saturation in the emission of signal QDs immobilized in 20% polyacrylamide gel as the laser intensity is increased (Fig. 2*E*). In addition, the blinking of the QDs became more prominent at increased illumination intensity (Movie S2). In contrast, increasing the laser intensity shone on $BaTiO_3$ nanocrystals resulted in an increase in the SHG intensity that rises quadratically (Fig. 2*C*). Note that the SHG signal of $BaTiO_3$ nanocrystals gets more than 2 orders of magnitude stronger as the illumination intensity is increased 40-fold. Increasing the illumination further resulted in even higher SHG intensities, well above optimal photomultiplier gain settings. The absence of $BaTiO_3$ nanocrystal saturation at higher light levels makes it possible for SHG nanoprobes to outperform even the brightest fluorescent dyes by increasing power levels (Fig. 2*D*) so long as the illumination remains below the damage threshold. Thus, SHG nanoprobes offer a means to record the signal from even single probes without compromising on spatiotemporal resolution by simply increasing the illumination power.

**Autofluorescence.** A major challenge for in vivo imaging in intact cells, tissues, or embryos is to collect selectively the signal from the label, with minimal contribution from tissue autofluorescence. The narrow bandwidth of the SHG signal (<5 nm with the laser employed) suggest that well-matched emission filters could be employed in the TPLSM to reject autofluorescence without sacrificing the collection of the entire SHG signal. We tested this property by immobilizing the nanoprobes in an optically challenging, scattering environment (2.5% Intralipid/0.05%

Indian Ink/20% polyacrylamide gel) simulating the scattering and absorption values of biological tissues (31). The SNR of the signal from the $BaTiO_3$ was significantly improved by replacing the broad emission filter (bandwidth ~70 nm) with a narrow (~10 nm) bandwidth emission filter (Fig. 3 *A*, *A′*, and *C*). In contrast, the signal and SNR from QDs were compromised by a narrower emission filter, which removed not only the autofluorescence but also a significant fraction of the broader emission from the QDs (Fig. 3 *B*, *B′*, and *D*).

**Live Imaging.** To test whether SHG nanoprobes can be detected in live vertebrate tissue, $BaTiO_3$ nanocrystals were injected into one-cell stage zebrafish embryos. Embryos are ideal for testing for even subtle effect on the health of cells as the cells are dividing rapidly and the labeled cells will be noticeably enlarged if their development is in any way slowed. The injected embryos developed indistinguishably from their uninjected counterparts (see *SI Materials and Methods*), demonstrating that $BaTiO_3$ is physiologically inert and nontoxic to the sensitive zebrafish embryonic cells.

The $BaTiO_3$ nanocrystals showed excellent long-term photostability when imaged in vivo. Such stability is particularly important for the analysis of biological processes such as tracking cell lineages or monitoring the dynamics of molecules within single cells. $BaTiO_3$ nanoparticles, coinjected with Dextran-Alexa546 into single cells at the 32-cell stage of zebrafish embryos, were imaged at the dome stage. The Alexa dye bleached quickly, making it hard to track the labeled cells over the hours of embryonic development; in contrast, $BaTiO_3$ showed no decrease in signal during the imaging session (Fig. S3), allowing long-term cell tracking.

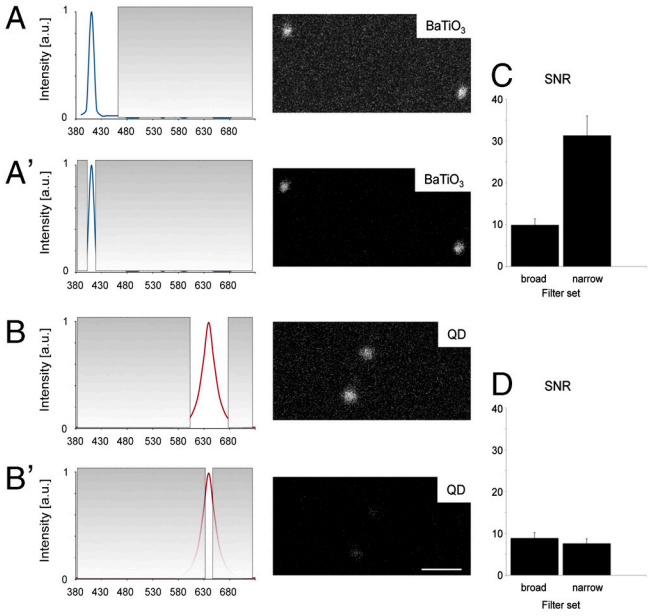


**Fig. 3.** SHG nanoprobes can be imaged with high SNR and virtually no signal background (*A–D*). Using optimized emission filter sets SHG nanoprobes provide superior SNR in highly scattering and absorbing environments. $BaTiO_3$ nanocrystals (*A* and *A′*) and water-soluble CdSe/ZnS quantum dots (*B* and *B′*) were immobilized in 2.5% Intralipid/0.05% Indian Ink/20% polyacrylamide gel, illuminated with 15% of 820-nm light, and respective signal intensity recorded either with a long (*A* and *B*) or a narrow (*A′* and *B′*) bandpass emission filter. The SNR for $BaTiO_3$ nanoparticles improves in this particular case 3-fold when a narrow emission filter is used (*C*) blocking most background signal from random absorption due to intense scattering, yet allowing transmission of a major part of SHG signal (*A′*, image). The SNR for QDs however cannot be increased when a narrow filter is used (*D*). In this case not only the background signal, but also the signal emission is significantly reduced (*B′*, image). Consequently, only $BaTiO_3$ can be imaged with virtually no background signal while in parallel increasing the SNR. (*A–B′*) Gray areas in the emission spectra of $BaTiO_3$ (blue line) and QDs (red line) indicate blocked transmission by emission filters. (*C* and *D*) The SNR columns represent the means ± range of two measurements each. Bar = 500 nm.

During development, a bright signal could be detected both from cells that were either superficial or deep within the zebrafish tissues. Even in deep tissues and organs, the imaging required only low levels of illumination intensity. The in vivo SHG intensity spectra were identical to those obtained in vitro. Unlike fluorescent probes, where the apparent emission spectrum is shifted by the greater loss of shorter wavelengths, the narrow SHG spectrum was merely attenuated rather than altered as nanocrystals deeper in the tissues were imaged. Using a narrow emission filter, SHG nanoprobes could be identified in the zebrafish trunk with an excellent SNR and virtually no background signal (Fig. 4 *B* and *C*, Movie S3, and Fig. S4 *A* and *B*).

The SHG from the nanocrystals was easily differentiated from the endogenous SHG from muscle fibers; the endogenous SHG was much weaker and was predominantly forward-propagated. It was best detected with the transdetector of the microscope and required at least 10 times greater illumination power when compared to the dimmest diffraction-limited SHG nanocrystal signal spots, representing presumably single SHG nanocrystals (Fig. 4 *B* and *C*). Similarly, the SHG from the nanocrystals was easier to excite and to detect in the epidetectors in comparison to collagen fibrils in mouse connective tissue (Fig. S4 *C* and *D*). Endogenous SHG could be sensed in the epidetector, but this signal was always weaker, as it represented the forward-generated SHG signal that must be back scattered to reach the objective lens. SHG from the nanoprobes could be detected in both trans- and epidirection (Fig. 4 *B–C*). The multidirectional SHG signal, which has been recently suggested for other particles (32, 33), allows the imaging of SHG nanoprobes with a TPLSM without any microscope modification.

**Immunostaining with SHG Nanoprobes.** To test whether functionalized $BaTiO_3$ nanocrystals can be used in immunostainings, we linked them to Cy5-tagged secondary antibodies using a protocol developed for antibody-conjugated QDs (34) (see *SI Materials and Methods*). Immunostaining by SHG nanoprobes confirmed the previous results of embryonic zebrafish Dystrophin protein localization (35). Both SHG- and Cy5-immunostaining label the muscle attachments within the myotome (Fig. 5); however, the Cy5-labeling displays a higher level of background binding of the fluorochromes not observed for the SHG nanoprobes. High detection contrast and selective attachment to biological molecules will offer insights into the dynamics of various biological targets and provide strategies for ultrasensitive molecular diagnostic reagents.

In conclusion, SHG nanoprobes offer unique advantages for molecular imaging studies due to their photophysical properties. The SHG from $BaTiO_3$ nanocrystals are not subject to the bleaching, blinking, and saturation that are unavoidable with the fluorescent agents currently used to characterize biological targets. Recently, nonblinking quantum dots have been introduced (20). However, this improvement sacrifices some of the QDs other advantages due to their broad, multipeaked emission spectrum, which limits potential biological in vivo applications, such as multicolor imaging and results in decreased SNR compared to conventional, yet blinking, QDs. In contrast, the narrow emission spectrum of SHG nanoprobes (<5 nm FWHM) allows experiments characterizing molecular targets with excellent sensitivity and superior SNR. The absence of an excited state lifetime and the ability to use brighter illumination to generate more signal permits SHG nanoprobes to offer a window into time regimes of molecular targets to which other techniques are blind. Because SHG nanoprobes don't bleach and saturate, dynamic analysis of different biological processes can be performed with fast acquisition rates of indefinite length. The SHG nanoprobes have been stable and nontoxic, without the need for a surface shell, avoiding

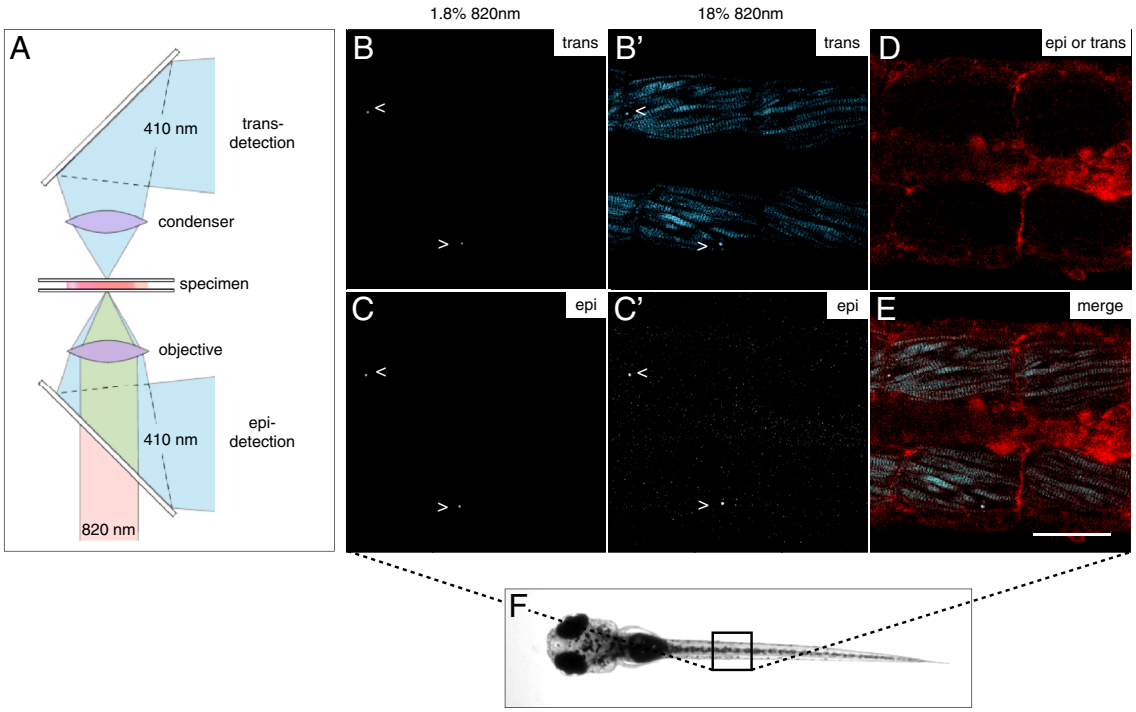


**Fig. 4.** SHG nanoprobes provide superior signal-to-noise ratio after in vivo injections $BaTiO_3$ nanocrystals were injected into one-cell stage zebrafish embryos. Several days after cytoplasmic injection (around 72 hpf) excitation of nanocrystals with femtosecond pulsed 820-nm light results in strong SHG signal detectable in epidirection as well as in transdirection (*A*) throughout the whole zebrafish body [here, nanocrystals (arrowheads) present in the trunk of a zebrafish (*B*–*C*)]. Endogenous SHG from trunk muscles can only be detected in transdirection with the sarcomere repeat patterns clearly observable (*B*). (*D*) BODIPY TR methyl ester dye labeling the extracellular matrix and cell membranes. (*E*) Merge of pictures *B*, *C*, and *D*. Note that the power levels required to detect endogenous SHG are 10 times higher than those to visualize $BaTiO_3$. The SHG signal intensity of $BaTiO_3$ is comparable in epi- as well as in transdetection mode. Anterior to the left. Bar = 75 μm.

one of the potential pitfalls of cadmium-containing QDs; recent work indicates that even robust coatings do not prevent subsequent breakdown of QDs in vivo (36). Future broad surveys of nonlinear optical nanomaterials possessing high conversion efficiencies with different optimal wavelengths within the well-known tissue "transparency window" of 600–1300 nm (37) will enable deep tissue multilabel colocalization imaging and the detection of multiple distinct target populations in parallel. Because SHG is a coherent process, three-dimensional molecular orientation analysis with high spatial resolution can be performed (38). Thus, SHG nanoprobes offer a window into the spatial and temporal dynamics of various biological targets at the molecular level with unmatched sensitivity and temporal resolution for both molecular imaging and molecular diagnostics (39).

## Materials and Methods

**Zebrafish.** Raising, maintaining, and spawning of wild-type and colorless (cls) mutant zebrafish were performed as previously described (40).

**Reagents.** Nonlinear crystals were obtained from commercial sources: 20 nm ZnO nanocrystals, 50–80 nm SiC nanocrystals, and 30 and 90 nm $BaTiO_3$ nanocrystals were purchased from Nanostructured and Amorphous Materials, Inc. and Techpowder. Water-soluble dark-red CdSe/ZnS core-shell quantum dots [approximately 30 nm in diameter, where the hydrodynamic size is about 2–3 times the dry radii (41)] were purchased from NN-Labs, LLC.

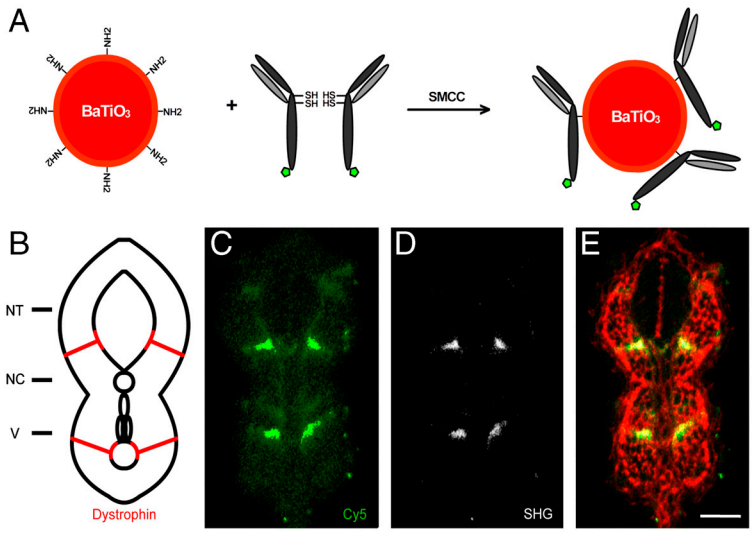


**Fig. 5.** SHG nanoprobe targeting specificity. (*A*) Scheme of SHG nanoprobe conjugation to Cy5-coupled (green pentagon) antibody fragments via disulphide reduction and sulfhydryl-amine coupling. (*B*) Schematic representation of a transversal section of trunk of a 24 hpf zebrafish embryo showing Dystrophin protein localization to fiber ends (red). NT, neural tube; NC, notochord; V, vessels. (*C*–*E*) Immunostaining showing Dystrophin protein localization in a transversal tissue section using secondary antibody coupled to Cy5 (green) and $BaTiO_3$ (white). Both readouts—Cy5 immunofluorescence (*C*), and $BaTiO_3$ SHG signal (*D*)—label specifically Dystrophin. (*E*) Phalloidin labeling (red) is superimposed to show cell profiles in the transversal tissue section. Note that SHG immunostaining provides superior SNR of Dystrophin detection using a narrow emission filter. Bar = 30 μm.

Intralipid-20% and Indian Ink solutions were purchased from Sigma-Aldrich Co. and Boston BioProducts, Inc.

**$BaTiO_3$ Nanocrystal Characterization.** For the SEM analysis, less than 1 mL of $BaTiO_3$ solution was deposited onto a piece of silicon on insulator (SOI) wafer, mounted onto an SEM stub. The SOI wafer was electrically grounded to the SEM stub using copper tape. An FEI Qanta SEM was employed to generate images of substrate topography. Images were generated with auto-contrast and auto-brightness settings.

Before each analysis (spectrum, blinking property comparison, and signal saturation comparison) SHG nanomaterial solutions were ultrasonicated, nanofiltered, and immobilized in 20% polyacrylamide gel. The spectrum was analyzed with the META detector of the Zeiss 510NLO microscope. To assay blinking of $BaTiO_3$ and water-soluble QD, both immobilized nanomaterials were imaged 300 times (20 frames/s) using a $40\times/1.3$ oil objective on a Zeiss 510NLO microscope. A mode-locked infrared laser line at 820 nm was used, originating from a Ti::Sapphire laser (Coherent, Inc.). The background value was set to zero and each obtained dataset was normalized accordingly. Data were analyzed using the Zeiss LSM software.

For the signal saturation comparison between $BaTiO_3$ and water-soluble QD, both immobilized nanomaterials were illuminated rapidly 5 times each (in particular to minimize fluctuating intensity values for blinking QDs) with increasing (up to 40-fold) 820-nm light intensity ($n = 4$). Data of nanocrystals and QDs having intensity values within the optimal photomultiplier gain setting were recorded and analyzed using the Zeiss LSM software.

**Signal-to-Noise Ratio Analysis of $BaTiO_3$ and QDs in Optically Challenging Environments.** To investigate the achievable SNR of $BaTiO_3$ versus water-soluble QD in optically challenging environments, we developed a phantom medium to simulate the distribution of light in tissue. The optical properties of different concentrations of Intralipid and Indian Ink have been previously studied (42, 43). $BaTiO_3$ and water-soluble QD were both immobilized in 2.5% Intralipid/0.05% Indian Ink/20% polyacrylamide and imaged using an long-distance correction ring apochromat objective (LD C-APO) $40\times/1.1$ objective either with a wide or a narrow bandpass emission filter (BaTiO: $\sim$410/70 nm and $\sim$410/10 nm; QD: $\sim$645/70 nm and $\sim$645/10 nm) by adjusting the META detector of the Zeiss 510NLO microscope setup. The filter setting selection was chosen such that minimizing the background signal should increase the SNR. The highest achievable SNR value of QDs served as the wide bandpass filter setting. In both cases, the same excitation power of 15% 820 nm was applied with comparable detection settings. Similar SNR values were achieved for QD when excited with 633 nm. Data were processed using the Zeiss LSM software and quantified using ImageJ (National Institutes of Health).

**ACKNOWLEDGMENTS.** We thank Le Trinh, Luca Caneparo, Thai Truong, Nathan Hodas, and William Dempsey for comments on the manuscript, Willy Supatto and William Dempsey for help with Matlab, David Koos for mouse tail preparation, and Demetri Psaltis for providing functionalized nanoprobes. Research was in part carried out at the Molecular Materials Research Center of the Beckman Institute of the California Institute of Technology. P.P. is supported by a German Science Foundation (Deutsche Forschungsgemeinschaft) Postdoctoral Fellowship. Supported by the Bio-Imaging Center at the California Institute of Technology, the National Human Genome Research Institute Center of Excellence in Genomic Science Grant P50HG004071, and the City of Hope/California Institute of Technology Initiative.

1. Prasher DC, Eckenrode VK, Ward WW, Prendergast FG, Cormier MJ (1992) Primary structure of the *Aequorea victoria* green-fluorescent protein. *Gene* 111(2):229–233.
2. Shaner NC, Steinbach PA, Tsien RY (2005) A guide to choosing fluorescent proteins. *Nat Methods* 2(12):905–909.
3. Lippincott-Schwartz J, Snapp E, Kenworthy A (2001) Studying protein dynamics in living cells. *Nat Rev Mol Cell Biol* 2(6):444–456.
4. Hadjantonakis AK, Dickinson ME, Fraser SE, Papaioannou VE (2003) Technicolour transgenics: Imaging tools for functional genomics in the mouse. *Nat Rev Genet* 4(8): 613–625.
5. Baskin JM, et al. (2007) Copper-free click chemistry for dynamic in vivo imaging. *Proc Natl Acad Sci USA* 104(43):16793–16797.
6. Datta D, Wang P, Carrico IS, Mayo SL, Tirrell DA (2002) A designed phenylalanyl-tRNA synthetase variant allows efficient in vivo incorporation of aryl ketone functionality into proteins. *J Am Chem Soc* 124(20):5652–5653.
7. Billinton N, Knight AW (2001) Seeing the wood through the trees: A review of techniques for distinguishing green fluorescent protein from endogenous autofluorescence. *Anal Biochem* 291(2):175–197.
8. Boyd RW (2003) *Nonlinear Optics* (Academic, San Diego), 2nd Ed, pp 1–117.
9. Sutherland RL, McLean DG, Kirkpatrick S (2003) *Handbook of Nonlinear Optics* (Dekker, New York), 2nd Ed, pp 1–336.
10. Campagnola PJ, Loew LM (2003) Second-harmonic imaging microscopy for visualizing biomolecular arrays in cells, tissues and organisms. *Nat Biotechnol* 21(11):1356–1360.
11. Pantazis P, Gonzalez-Gaitan M (2007) Localized multiphoton photoactivation of paGFP in Drosophila wing imaginal discs. *J Biomed Opt* 12(4):044004 1–7.
12. Nikogosyan DN (2005) *Nonlinear Optical Crystals: A Complete Survey* (Springer-Science, New York), pp 5–391.
13. Bonacina L, et al. (2007) Polar Fe (IO 3) 3 nanocrystals as local probes for nonlinear microscopy. *Appl Phys B: Lasers Opt* 87(3):399–403.
14. Kachynski A, Kuzmin A, Nyk M, Roy I, Prasad P (2008) Zinc oxide nanocrystals for non-resonant nonlinear optical microscopy in biology and medicine. *J Phys Chem C* 112(29):10721–10724.
15. Hsieh CL, Grange R, Pu Y, Psaltis D (2009) Three-dimensional harmonic holographic microcopy using nanoparticles as probes for cell imaging. *Opt Express* 17(4): 2880–2891.
16. Supatto W, Debarre D, Farge E, Beaurepaire E (2005) Femtosecond pulse-induced microprocessing of live Drosophila embryos. *Med Laser Appl* 20(3):207–216.
17. Denk W, Strickler JH, Webb WW (1990) Two-photon laser scanning fluorescence microscopy. *Science* 248(4951):73–76.
18. Bruchez M, Jr, Moronne M, Gin P, Weiss S, Alivisatos AP (1998) Semiconductor nanocrystals as fluorescent biological labels. *Science* 281(5385):2013–2016.
19. Chan WC, Nie S (1998) Quantum dot bioconjugates for ultrasensitive nonisotopic detection. *Science* 281(5385):2016–2018.
20. Wang X, et al. (2009) Non-blinking semiconductor nanocrystals. *Nature* 459(7247): 686–689.
21. Huang MZ, Ching WY (1993) Calculation of optical excitations in cubic semiconductors. II. Second-harmonic generation. *Phys Rev B Condens Matter* 47(15):9464–9478.
22. Dickson RM, Cubitt AB, Tsien RY, Moerner WE (1997) On/off blinking and switching behaviour of single molecules of green fluorescent protein. *Nature* 388(6640): 355–358.
23. Pelton M, Smith G, Scherer NF, Marcus RA (2007) Evidence for a diffusion-controlled mechanism for fluorescence blinking of colloidal quantum dots. *Proc Natl Acad Sci USA* 104(36):14249–14254.
24. Dahan M, et al. (2003) Diffusion dynamics of glycine receptors revealed by single-quantum dot tracking. *Science* 302(5644):442–445.
25. Stollberg J, Fraser SE (1988) Acetylcholine receptors and concanavalin A-binding sites on cultured Xenopus muscle cells: Electrophoresis, diffusion, and aggregation. *J Cell Biol* 107(4):1397–1408.
26. Nirmal M, et al. (1996) Fluorescence intermittency in single cadmium selenide nanocrystals. *Nature* 383(6603):802–804.
27. Basche T (1998) Fluorescence intensity fluctuations of single atoms, molecules and nanoparticles. *J Lumin* 76–77:263–269.
28. Empedocles SA (1999) Influence of spectral diffusion on the line shapes of single CdSe nanocrystallite quantum dots. *J Phys Chem B* 103(11):1826–1830.
29. Michler P, et al. (2000) Quantum correlation among photons from a single quantum dot at room temperature. *Nature* 406(6799):968–970.
30. Bannai H, Levi S, Schweizer C, Dahan M, Triller A (2007) Imaging the lateral diffusion of membrane molecules with quantum dots. *Nat Protoc* 1(6):2628–2634.
31. Cheong WF, Prahl SA, Welch AJ (1990) A review of the optical properties of biological tissues. *IEEE J Quantum Elect* 26(12):2166–2185.
32. Pavlyukh Y, Hübner W (2004) Nonlinear Mie scattering from spherical particles. *Phys Rev B* 70(24):1–8.
33. Shan J, Dadap JI, Stiopkin I, Reider GA, Heinz TF (2006) Experimental study of optical second-harmonic scattering from spherical nanoparticles. *Phys Rev A* 73(2): 023819–023814.
34. Xing Y, et al. (2007) Bioconjugated quantum dots for multiplexed and quantitative immunohistochemistry. *Nat Protoc* 2(5):1152–1165.
35. Parsons MJ, Campos I, Hirst EM, Stemple DL (2002) Removal of dystroglycan causes severe muscular dystrophy in zebrafish embryos. *Development* 129(14):3505–3512.
36. Fitzpatrick JA, et al. (2009) Long-term persistence and spectral blue shifting of quantum dots in vivo. *Nano Lett* 9(7):2736–2741.
37. Tromberg BJ, et al. (2000) Non-invasive in vivo characterization of breast tumors using photon migration spectroscopy. *Neoplasia* 2(1–2):26–40.
38. Pu Y, Centurion M, Psaltis D (2008) Harmonic holography: A new holographic principle. *Appl Opt* 47(4):A103–110.
39. Weissleder R, Pittet MJ (2008) Imaging in the era of molecular oncology. *Nature* 452(7187):580–589.
40. Westerfield M (1995) *The Zebrafish Book* (Univ of Oregon Press, Eugene, OR), 3rd Ed, pp 1–385.
41. Larson DR, et al. (2003) Water-soluble quantum dots for multiphoton fluorescence imaging in vivo. *Science* 300(5624):1434–1436.
42. van Staveren HJ, Moes CJM, van Marie J, Prahl SA, van Gemert MJC (1991) Light scattering in Intralipid-10% in the wavelength range of 400–1100 nm. *Appl Opt* 30(31):4507–4514.
43. Madsen SJ, Patterson MS, Wilson BC (1992) The use of India ink as an optical absorber in tissue-simulating phantoms. *Phys Med Biol* 37(4):985–993.